

# Mountains to climb: on the role of seamounts in upwelling deep-ocean waters through turbulent mixing

Ali Mashayek<sup>1</sup>, Jonathan Gula<sup>2,3</sup>, Lois E. Baker<sup>4</sup>, Alberto C. Naveira Garabato<sup>5</sup>, Laura Cimoli<sup>6</sup>, James J. Riley<sup>7</sup>, and Casimir de Lavergne<sup>8</sup>

This manuscript was compiled on May 8, 2024

Turbulent mixing in the ocean exerts an important control on the rate and structure of the overturning circulation. However, the balance of processes underpinning this mixing is subject to significant uncertainties, limiting our understanding of the overturning's deep upwelling limb. Here, we investigate the hitherto primarily neglected role of tens of thousands of seamounts in sustaining deep-ocean upwelling. Dynamical theory indicates that seamounts may stir and mix deep waters by generating lee waves and topographic wake vortices. At low latitudes, stirring and mixing are predicted to be enhanced by a layered vortex regime in the wakes. Using three realistic regional simulations spanning equatorial to middle latitudes, we show that layered wake vortices and elevated mixing are widespread around seamounts. We identify scalings that relate mixing rate within seamount wakes to topographic and hydrographic parameters. We then apply such scalings to a global seamount dataset and an ocean climatology to show that seamount-generated mixing makes an important contribution to the upwelling of deep waters. Our work thus brings seamounts to the fore of the deep-ocean mixing problem and urges observational, theoretical and modelling efforts toward incorporating the seamounts' mixing effects in conceptual and numerical ocean circulation models.

Seamounts | Wakes | Vortices | Mixing | Upwelling

Turbulence at centimetre scales plays a pivotal role in shaping the overturning circulation of the deep ocean (1, 2), as well as the ocean's capacity to distribute and store climate-critical tracers (3, 4). As dense, deep water masses flow away from their high-latitude formation regions, small-scale turbulence induces mixing with surrounding layers, leading to a net transfer of water across isopycnals. These transfers regulate the rate and structure of deep-ocean overturning (5–7) and, in so doing, influence the oceanic inventories and turnover time scales of heat, carbon and other important biogeochemical substances.

Decades of research in ocean mixing have brought a solid understanding of the key energy sources of turbulent mixing (winds, tides, and geothermal heating through the seafloor) (1, 8), and of a wide range of mechanisms of small-scale turbulence generation (9, 10). However, several major knowledge gaps remain. Possibly chief amongst these is the uncertain role of turbulent processes near the ocean's bottom boundary (11, 12). These processes have been argued to potentially account for the bulk of deep-ocean upwelling (1, 2) but, with few targeted observations, comparatively little is known about their nature and large-scale impacts.

Most past investigations of turbulent mixing near the bottom boundary have examined contributions from either the breaking of internal waves (following the waves' generation, reflection or scattering at the boundary; see (9) for a recent review), or a range of complex non-wave processes in topographically-constrained canyons and passages (e.g., hydraulic jumps at sills) (13, 14). More recently, the focus has shifted increasingly to a distinct class of phenomena underpinning near-boundary mixing: submesoscale instabilities (15–20). These instabilities develop as quasi-geostrophic flows over sloping topography generate a reversal in the sign of potential vorticity (a conserved property of geophysical fluids that can only be changed by frictional and diabatic processes) near the boundary and induce overturning motions that restore stability by mixing boundary and off-boundary waters. Intense near-bottom mixing by submesoscale instabilities has been documented in some regions with energetic mesoscale motions (e.g., the Gulf Stream (16) or a deep western boundary current in the Scotia Sea (18)), suggesting that these instabilities may be widely active mixing agents.

## Significance Statement

This research uncovers the crucial role of seamounts, underwater mountains, in influencing deep-ocean circulation. Seamounts stir and mix deep waters by generating waves and vortices, particularly in low-latitude regions. This study employs realistic simulations and identifies key parameters affecting mixing rates around seamounts. Applying these findings to a global seamount dataset, the research demonstrates that seamount-generated mixing significantly contributes to the upwelling of deep waters. This discovery challenges previous understanding and emphasizes the need to incorporate seamount effects in ocean circulation models. By shedding light on this previously overlooked aspect, the study paves the way for more accurate representations of ocean dynamics and ultimately advances our comprehension of Earth's complex climate system.

Author affiliations: <sup>1</sup>Department of Earth Sciences, University of Cambridge, UK; <sup>2</sup>Univ Brest, CNRS, IRD, Ifremer, INRIA, Laboratoire d'Océanographie Physique et Spatiale (LOPS), IUEM, Brest, France; <sup>3</sup>Institut Universitaire de France (IUF), Paris, France; <sup>4</sup>School of Mathematics and Maxwell Institute for Mathematical Sciences, University of Edinburgh, UK; <sup>5</sup>University of Southampton, Southampton, UK; <sup>6</sup>Department of Applied Mathematics and Theoretical Physics, University of Cambridge, Cambridge, UK; <sup>7</sup>University of Washington, Seattle, USA; <sup>8</sup>LOCEAN Laboratory, Sorbonne Université-CNRS-IRD-MNHN, Paris, France

125 Yet, as common as these instabilities might be, fresh  
126 theoretical advances emphasize the potential prevalence of  
127 a largely neglected, more generic form of mesoscale flow-  
128 topography interaction, which encompasses and broadens  
129 most scenarios of submesoscale instability development:  
130 the generation of topographic wakes (21). These wakes  
131 are produced when the highly-sheared near-boundary flow  
132 separates from sloping topography and moves into the oceanic  
133 interior (21). Flow separation need not always be associated  
134 with a reversal in the sign of potential vorticity close to the  
135 boundary, but may be readily enabled by the boundary's  
136 geometry (15) or the background mesoscale strain field (22).  
137 Upon escaping the boundary's constraint, the separated,  
138 sheared flow undergoes a variety of instabilities, which lead to  
139 both elevated turbulent mixing in the wake (16, 23–25) and  
140 the generation of submesoscale vortical filaments (15, 26, 27).

141 Where, then, might we expect topographic wakes to induce  
142 vigorous turbulent mixing in the deep ocean? Although wake  
143 generation can potentially occur at various types of sloping  
144 topography, the most common form of such topography is  
145 provided by isolated volcanic seamounts – of which some  
146 tens to hundreds of thousands with heights of hundreds  
147 of metres or taller are estimated to exist (28–30). Thus,  
148 in this work, we combine the latest developments in our  
149 theoretical understanding of wake generation with a global  
150 seamount census to perform a baseline assessment of the role  
151 of topographic wakes in sustaining deep-ocean mixing and  
152 upwelling. This allows us to address the fundamental question  
153 posed initially by Munk & Wunsch (8): “Are seamounts and  
154 islands the stirring rods of the oceans?”

## 155 Global Seamount Census

156 Our analysis is founded on the seamount dataset of Kim  
157 & Wessel (31, hereafter KW11), which includes ~25,000  
158 seamounts with heights over 100 m in areas away from  
159 continental margins. Approximately 8,500 of these seamounts  
160 are taller than 1 km. KW11 predict that their database likely  
161 underestimates the global inventory of seamounts by nearly a  
162 factor of two; this is confirmed by Gevorgian *et al.* (32), who  
163 updated the total number to 43,454 seamounts. Thus, the  
164 KW11 database is conservative, as it includes a significantly  
165 lower number of seamounts than other predictions. For  
166 example, Wessel *et al.* (28) reported more than 100,000  
167 seamounts with heights exceeding 1 km, and speculated  
168 that there are probably 25 million seamounts taller than  
169 100 m. Similarly, Yesson *et al.* (29) reported ~140,000  
170 seamounts with peak heights between 500 m and 1 km, and  
171 ~ 33,500 seamounts taller than 1 km. The KW11 data  
172 incorporates corrections for the ambiguity in gravity signals  
173 due to small seamounts and for the overlap with abyssal  
174 hills, which are typically 100 m high on a horizontal scale  
175 <10 km, and most prevalent along mid-ocean ridges (33).  
176 As a result, seamounts captured by the KW11 data are  
177 distinct from abyssal hills and correspond instead to active  
178 or extinct undersea volcanoes (of isolated or combination  
179 conical shapes) with heights over 100 m. It is worth noting  
180 that in the realistic simulations performed in this study, each  
181 using high-resolution bathymetry derived from multi-beam  
182 surveys, there are multiple examples of seamounts that are  
183 not found in the KW11 seamount census, emphasizing the  
184 conservative seamount count of KW11. Figure 1b shows the  
185

186 global distribution of the KW11 seamounts, coloured by their  
187 height. For reference, the seafloor depth is shown in Figure  
188 1a.

## 189 Flow Around a Seamount

190 A flow past a seamount generates a turbulent topographic  
191 wake with patches of both cyclonic and anticyclonic vorticity,  
192 leading to instabilities and formation of submesoscale coherent  
193 vortices (SCVs) with either sign of vorticity in the wake of the  
194 seamount (26, 27, 36, 37). While two-dimensional (2D) wake  
195 flow past a cylinder is a classic problem in fluid mechanics,  
196 the description of 3D seamount wakes in a rotating density-  
197 stratified ocean is a recently attacked and more complex  
198 problem. The impacts of rotation and stratification on wake  
199 dynamics can be encapsulated in two dimensionless numbers:  
200 the Rossby number  $Ro = \frac{U}{fD}$ , and the Froude number  $Fr =$   
201  $\frac{U}{NH}$ , where  $U$  is the horizontal velocity,  $f$  is the Coriolis  
202 frequency,  $N$  is the buoyancy frequency,  $H$  is the height of  
203 the seamount, and  $D$  is the diameter of the seamount at  
204 its mid-height. The Froude number gives the ratio of the  
205 energetically possible amplitude of vertical fluid displacement  
206 to the seamount height. A small Froude number ( $Fr < 1$ )  
207 implies that the flow skirts most of the height of the seamount  
208 and leads predominantly to the generation of wake vortices,  
209 although lee wave generation still occurs from the top portion  
210 of the seamount, which has effective height  $\sim U/N$  (Fig.  
211 1d) (38, 39). In contrast, a large Froude number ( $Fr >$   
212 1) describes a lee wave-dominated regime with a most of  
213 the flow directed over rather than around the seamount,  
214 resulting in relatively stronger generation of topographic lee  
215 waves than topographic wakes (39). We note that there  
216 exists extensive literature on flow over mountains in the  
217 atmospheric context (40, 41), but such flows often correspond  
218 to higher Froude numbers as compared to the oceanic flows  
219 over seamounts, and thus, the dynamics are dominated by  
220 lee wave generation, which is not our focus herein.

221 The vertical structure of wake vortices has been found to  
222 further depend on the ratio of Rossby and Froude numbers,  
223 expressed by the Burger number  $Bu = (Ro/Fr)^2 = (\frac{NH}{fD})^2$   
224 (26, 42). The Burger number can also be viewed as the  
225 (squared) ratio of an effective Rossby deformation radius  
226  $R_D \sim NH/f$  (where the seamount height  $H$  replaces the  
227 seafloor depth as the relevant vertical length scale) and the  
228 mid-height seamount diameter  $D$ . Small  $Bu$  values are  
229 associated with vertically coherent vortices (with horizontal  
230 scale set by the deformation radius), whereas large  $Bu$  values  
231 characterize layered vortices (with horizontal scale at a given  
232 depth set by the local seamount diameter at that depth)  
233 (26) – see Figure 1d. This latter case carries important  
234 implications for the generation of small-scale turbulence  
235 within the wakes, due to the strong vertical shear between  
236 the vortices' layers (27, 42). For small and moderate values  
237 of  $Ro$  and  $Bu$ , the turbulent mixing occurs predominantly  
238 in the anticyclonic region of the wake due to centrifugal  
239 (or inertial) instability (16, 23), eventually enhanced by the  
240 contribution of secondary wave emission from the unstable  
241 wake (21) and by the generation and trapping of near-inertial  
242 waves (24). However, large  $Bu$  and order one  $Ro$  values  
243 imply a transition to a more effective stratified turbulence  
244 regime driven by three-dimensional vertical shear instabilities  
245 in the wake (43). Hence, low-latitude topographic wakes may  
246

249  
250  
251  
252  
253  
254  
255  
256  
257  
258  
259  
260  
261  
262  
263  
264  
265  
266  
267  
268  
269  
270  
271  
272  
273  
274  
275  
276  
277  
278  
279  
280  
281  
282  
283  
284  
285  
286  
287  
288  
289  
290  
291  
292  
293  
294  
295  
296  
297  
298  
299  
300  
301  
302  
303  
304  
305  
306  
307  
308  
309  
310

311  
312  
313  
314  
315  
316  
317  
318  
319  
320  
321  
322  
323  
324  
325  
326  
327  
328  
329  
330  
331  
332  
333  
334  
335  
336  
337  
338  
339  
340  
341  
342  
343  
344  
345  
346  
347  
348  
349  
350  
351  
352  
353  
354  
355  
356  
357  
358  
359  
360  
361  
362  
363  
364  
365  
366  
367  
368  
369  
370  
371  
372

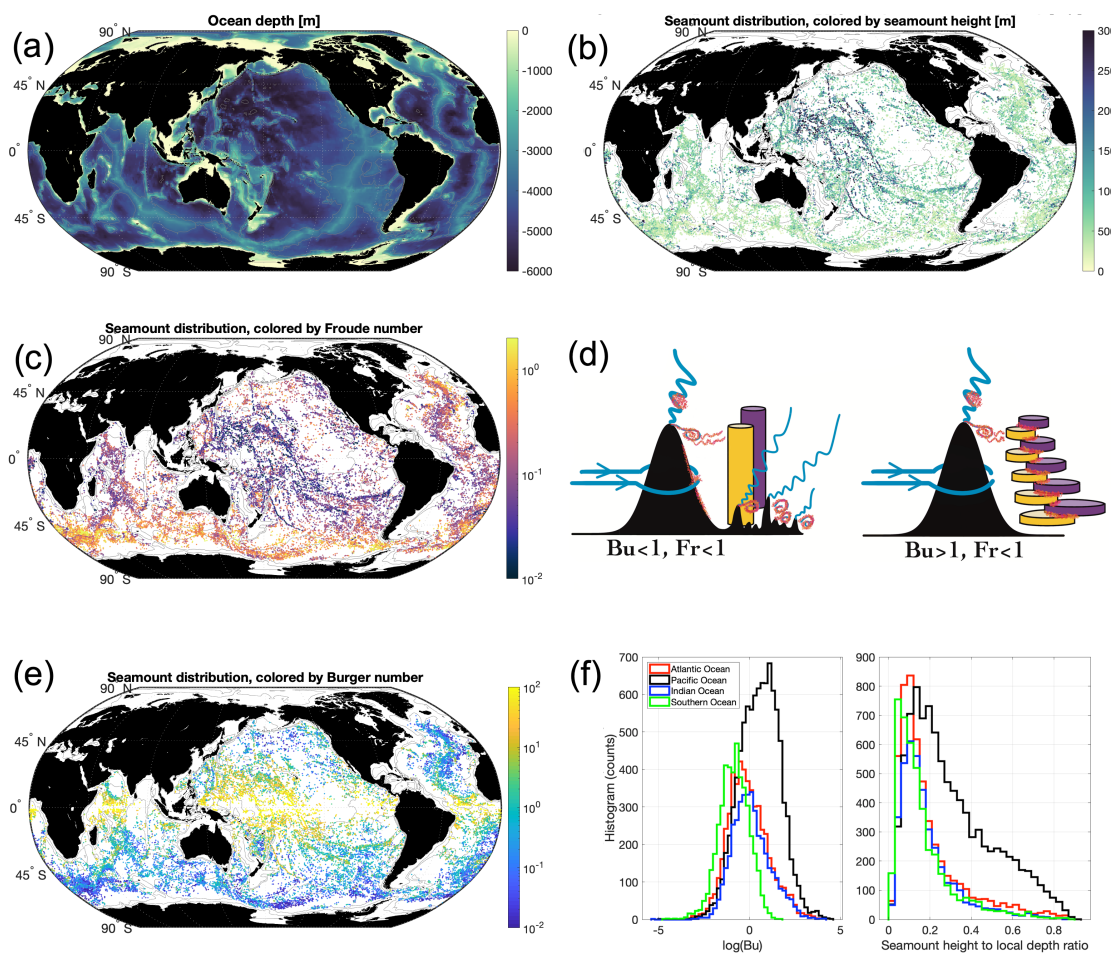


**Fig. 1.** (a) Ocean depth. (b) Global distribution of seamounts (from (31)), composed of  $\sim 25,000$  seamounts. (c) Same as panel b, but coloured based on the seamount Froude number. (d) A schematic summarizing the various dynamical paradigms of flow around seamounts as a function of Burger and Froude numbers. (e) Same as panel b, but coloured based on the seamount Burger number. (f) Histograms of seamount counts based on (left) their Burger numbers and (right) their height to basal-depth ratios, divided into different basins. A map of Rossby number for the seamounts is included in the Supporting Information. Burger and Froude numbers are defined based on seamount height and diameter from (31) and ambient stratification and velocity from (34, 35); see text for exact definitions and Supporting Information for further discussion and validation.

be expected to be particularly effective at generating small-scale turbulence, as the equatorward-decreasing  $f$  results in wake structures that are more vertically sheared and more susceptible to instability (43). The dependence on  $Bu$  of dynamical regimes of flow impingement on seamounts outlined here has been recently explored and corroborated with large eddy simulations (39, 42).

In this work, we set aside the lee wave radiation regime, which, despite its regional significance, has been investigated within earlier studies of lee wave generation over generalized rough topography (44, 45). We also exclude the influence of tides, as we find that the tidal excursion is generally small compared to the horizontal scale of the seamounts, such that the tidal flows are likely to be secondary to the mean flow in the generation of wake vortices (see Supporting Information). However, interactions between tides and seamounts can also be important for enhancing mixing (46, 47). Instead, our focus is on the turbulent mixing induced by vertically sheared layered vortices that form in the wake of seamounts throughout the world ocean, including potential secondary wave generation and trapping within the wake. To our knowledge, the basin-scale impacts of this regime of flow-seamount interaction have not been considered to date, yet, as we will see, these impacts are predicted to be important to global ocean circulation.

In Figure 1c, we construct a map of  $Fr$  based on the KW11 seamount data and estimated values of stratification  $N$  and flow speed  $U$ .  $N$  is estimated from climatological stratification (WOCE; 48), taken at the nearest vertical level and horizontal grid point to the KW11 seamount mid-depths.  $U$  is also taken at the KW11 seamount mid-depths, and is calculated from a field of root-mean-square flow speed from a 1/48° resolution ocean model simulation adapted from (49) (LLC4320, see Methods and Supporting Information). The dependence of  $Fr$  on flow speed highlights regions associated with intense flows, such as the Antarctic Circumpolar Current (ACC), western boundary currents, abyssal channels and passages, etc. The corresponding estimate of  $Bu$  is displayed in Figure 1e, illustrating that, overall, seamount wakes are expected to be more layered at low latitudes due to the inverse dependence of  $Bu$  on  $f$  – see also the distribution of seamounts in  $Fr - Ro$  space shown in Supporting Figure S3. At high latitudes (e.g., in the ACC region), flow impingement on seamounts is instead mostly predicted to generate barotropic vortices. Note, however, that substantial regional departures from this general pattern do occur, linked primarily to the seamount aspect ratio  $H/D$ .

A basin-by-basin histogram synthesis of the height to basal-depth (depth at the seamount base) ratio and  $Bu$  of the seamount field is provided by Figure 1f. The Pacific Ocean stands out because it hosts larger percentages of high- $Bu$  and tall (relative to the local seafloor depth) seamounts than other basins. The more frequent occurrence of high- $Bu$  regimes makes the Pacific Ocean particularly favourable to developing shear-induced turbulence associated with layered wake vortices. In contrast, the Southern Ocean seamounts are expected to mostly produce barotropic vortices, with the Atlantic and Indian basins falling in between the Pacific and Southern Ocean extremes. The Pacific Ocean's comparative richness of 'locally tall' seamounts further suggests

that seamount-induced dynamics in this basin may impact shallower waters than in the rest of the world's oceans.

Given the strong dependence of the wake structure on the Rossby and Froude numbers, and following diapycnal diffusivity and energy dissipation scalings by Perfect *et al.* (42) and Srinivasan *et al.* (43), we look for a scaling for the diapycnal diffusivity due to the seamount wake of the form:  $K_\rho = K_1 Fr^\alpha Ro^\beta$ .

Based on idealized numerical simulations of the flow around an isolated seamount immersed in constant stratification, Perfect *et al.* (42) reported that the domain-averaged diapycnal diffusivity follows the scaling:

$$K_\rho^{(1)} \sim K_0 (Fr Ro)^2, \quad [1]$$

for  $N < 10^{-3} \text{ s}^{-1}$ , with  $K_0 \approx 3 \text{ m}^2 \text{ s}^{-1}$ . The size of their simulation (and averaging) domain is 2.6 seamount basal diameters in the cross-stream direction, 3.8 basal diameters in the along-stream direction and 1.4 seamount height in the vertical. According to this simple scaling, the vortex-associated diffusivity  $K_\rho^{(1)}$  may exceed background turbulent levels in the ocean interior ( $\sim 10^{-5} \text{ m}^2 \text{ s}^{-1}$ ) for  $Fr Ro \geq 0.002$ , and can be as large as mixing rates in the most energetic tidal zones ( $\geq 10^{-3} \text{ m}^2 \text{ s}^{-1}$ ) for  $Fr Ro \geq 0.02$  (50). The scaling of Eq. 1 exhibits qualitative consistency with results from a recent numerical study of equatorial topographic wakes (43). However, it was developed within highly idealized scenarios and its quantitative predictive power might not encompass the diversity of realistic oceanographic regimes.

An alternative scaling is obtained using high-resolution realistic models of the ocean circulation in three paradigmatic regions: an equatorial area (representing the large- $Bu$  limit with strongly-sheared, layered topographic vortices); a low-latitude area over the Mid-Atlantic Ridge (including a wide range of seamounts and  $Bu$ ); and a mid-latitude case, in the seamount-rich area around the New England Seamount Rise (representing  $Bu$  just above unity; see Methods and Supporting Information for a detailed description of the simulations). We derive this scaling by using a non-linear least squares fit of the function  $K_\rho = K_1 Fr^\alpha Ro^\beta$  to the modelled diffusivities from the three high-resolution realistic models (suitably averaged around seamounts and excluding the deepest 100 m; see Supporting Information). Note that this fit was performed after selecting seamounts that meet the validity criteria of Eq. 1, which include  $Bu > 1$ ,  $Fr < 1$ , and  $Ro < 1$ , to focus on wake vortex regimes. The result is a function:

$$K_\rho^{(2)} \sim K_1 Fr^{1.7} Ro^{1.1}, \quad [2]$$

with  $K_1 = 0.6 \text{ m}^2 \text{ s}^{-1}$ . An interesting difference between the two scalings is the dependence on  $Ro$ , which is almost linear in Eq. 2 but quadratic in Eq. 1. This is an empirical result and (much) further research is required to fully understand the geophysical fluid dynamics of this problem.

Next, we assess the preceding theoretical framework and the validity of the two diapycnal diffusivity scaling relations by analyzing the seamount wakes and resulting diapycnal diffusivity in the three aforementioned high-resolution simulations, each corresponding to a typical dynamical regime. We will then apply the two scaling relations for the diapycnal diffusivity to the KW11 seamount data (Fig. 1b) and climatological stratification and flow speed data (Fig. 1c,e)

497 to assess the contribution of seamount-induced mixing to  
498 deep-ocean upwelling on a global scale.

499 **Equatorial Seamounts: an Example of Layered Vortices.** 500 The validity of the theoretical description of flow around  
501 a seamount in a realistic high- $Bu$  setting is first illustrated  
502 with a regional simulation in the equatorial Atlantic Ocean  
503 (Fig. 2; see Methods and Supporting Information for a  
504 detailed description of the simulation). Snapshots of relative  
505 vorticity at a vertical level (2800 m) intersected by seamounts  
506 (Fig. 2a) and along a vertical section crossing the model  
507 domain (Fig. 2b) reveal the occurrence of intense cyclonic  
508 and anticyclonic filaments and vortices in the wake of the  
509 seamounts, following a predominantly southeastward current  
510 below 1500 m (see also Supporting Movie S1). These features  
511 exhibit complex, vertically layered structures associated with  
512 intense vertical shear (Fig. 2e) and are thus expected to  
513 generate strong turbulent mixing. That the simulated wake  
514 vortices conform to theoretical predictions may be illustrated  
515 by estimating the set of dimensionless parameters on which  
516 the theory is founded. The modelled flows around the  
517 seamounts are characterized by a typical Rossby number  
518  $Ro \sim 1$ , a Froude number  $Fr \sim 0.01 - 0.1$ , and a Burger  
519 number  $Bu \sim 100 - 10,000$ . These correspond squarely to  
520 the layered wake vortex regime (Fig. 1d) and thereby indicate  
521 that the area should have a rich field of layered topographic  
522 vortices (43) – as indeed it is found to.

523 The simulation also supports the notion that seamounts  
524 can elevate bulk regional deep-ocean diffusivities by one order  
525 of magnitude or more (Fig. 2d). Specifically, the vertically  
526 sheared layers in the simulation give rise to high diffusivities of  
527 as much as  $O(10^{-3} - 10^{-2}) \text{ m}^2 \text{ s}^{-1}$  in the wakes of seamounts  
528 (Fig. 2f,g). These diffusivities exceed background mixing  
529 rates by one to two orders of magnitude below 1500 m depth  
530 (Fig. 2d) and are in the range of diffusivities predicted by the  
531 theoretical scaling (Fig. 2c). A comprehensive comparison  
532 of modelled and scaling-predicted diffusivities is provided in  
533 the Supporting Information.

534 **Mid-Atlantic Ridge and New England Seamounts: Examples  
535 of Hybrid Dynamics.** The Mid-Atlantic Ridge hosts seamounts  
536 with diverse radii, heights and depths, thus spanning a wide  
537 range of  $Bu$  values (Fig. 1e). A regional simulation of  
538 a portion of the Mid-Atlantic Ridge extending from 5°S  
539 to 12°S is used here to illustrate a seamount wake regime  
540 that is a hybrid of coherent and layered vortex regimes (Fig.  
541 3; see Methods and Supporting Information for a detailed  
542 description of the simulation). The impingement of mesoscale  
543 eddies on the seamounts generates a complex field of wake  
544 vortices, as revealed by a map of relative vorticity at 2800 m  
545 (Fig. 3a, see also Supporting Movie S2). A vertical section  
546 of relative vorticity further shows that these vortices can  
547 be vertically coherent in the interior yet highly sheared in  
548 the vicinity of topography (Fig. 3d). A vertical view of  
549 the modelled diapycnal diffusivity distribution indicates that  
550 turbulent mixing is enhanced within a few hundred meters  
551 of the seafloor or more around the wake vortices (Fig. 3h),  
552 with diffusivities approaching and exceeding  $O(10^{-3}) \text{ m}^2 \text{ s}^{-1}$   
553 tens of kilometers around seamounts.

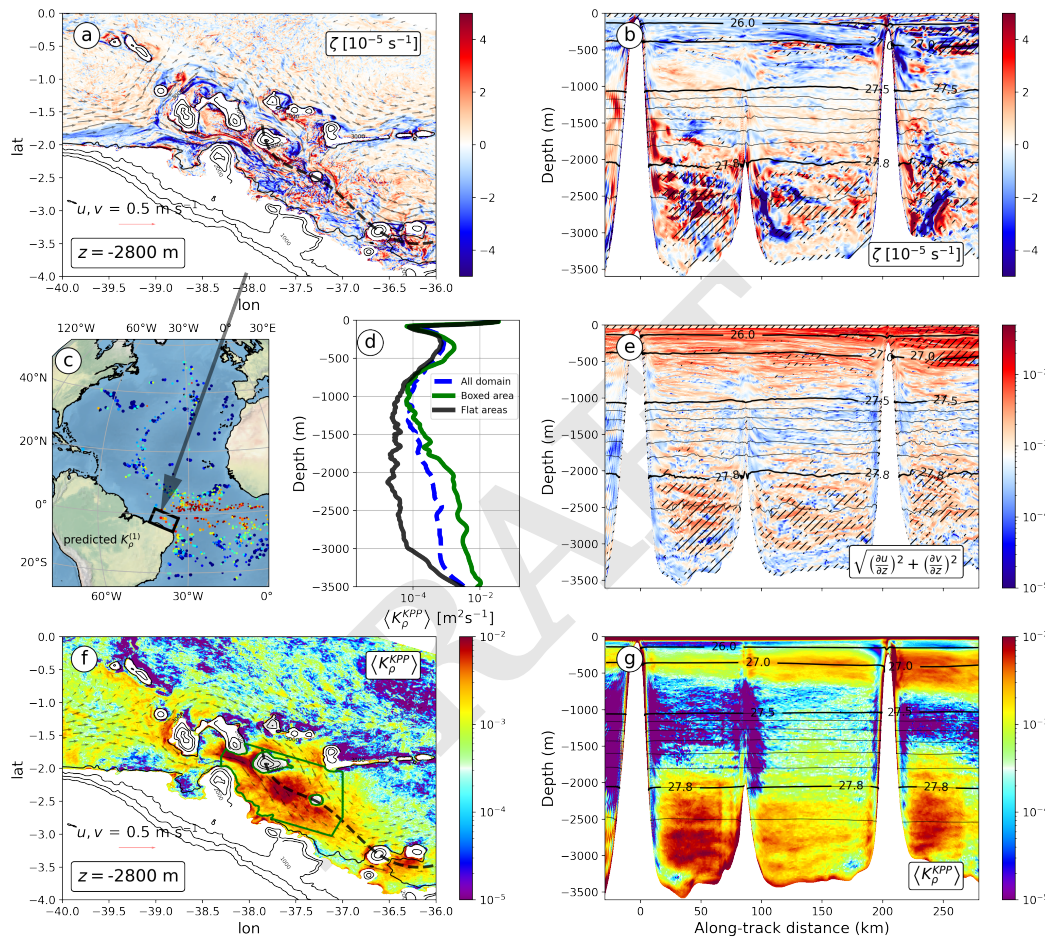
554 Cases with moderate  $Bu$  may also produce intense mixing.  
555 For example, numerical simulations of the New England  
556 seamounts – a chain of deep seamounts on the path of the Gulf

557 Stream – highlight the occurrence of intense turbulent wakes  
558 and high-amplitude lee waves in the lee of the seamounts  
559 (Fig. 3b,e). These wakes can extend horizontally up to 100  
560 km downstream and vertically from the bottom to slightly  
561 above the peak of the seamounts. The seamount shown in  
562 Fig. 3e has a shape similar to that of the idealized seamount  
563 studied by Perfect *et al.* (42), with characteristic values of  
564  $D = 25 \text{ km}$  for the half-width,  $H = 3000 \text{ m}$  for the height,  
565 and a background seafloor depth of 5000 m. Locally, the  
566 Coriolis parameter is  $f \sim 0.8 \times 10^{-4} \text{ s}^{-1}$ , and the mean  
567 stratification is  $N \sim 10^{-3} \text{ s}^{-1}$ , corresponding to a typical  
568 Rossby number  $Ro \sim 0.1$ , a Froude number  $Fr \sim 0.1$ , and a  
569 Burger number  $Bu \sim 2$ . The vortical wake structure is thus  
570 expected to be more vertically coherent than in the previous  
571 cases, as confirmed by the simulation (see Supporting Movie  
572 S3). The vortical wake is associated with an enhancement of  
573 turbulent mixing, again by one to two orders of magnitude  
574 relative to typical levels at the same depth away from the  
575 seamounts (Fig. 3i). In this case, the elevated diffusivities  
576 are localized predominantly on the anticyclonic side of the  
577 wake, as is characteristic of centrifugal instability in the near  
578 wake for extratropical cases with  $Ro < 1$  (43), but also show  
579 the signature of internal waves generated by the unstable  
580 wake and/or trapped inside by the anticyclonic side of the  
581 wake.

582 In all these examples the theoretical scaling from Eq. 1  
583 predicts diffusivities that display a wider range of values, with  
584 lower diffusivities for most seamounts and higher diffusivities  
585 for some high- $Bu$  seamounts (Supporting Figure S12 and  
586 Fig. 3f,g). On the other hand, the scaling from Eq. 2  
587 shows a better agreement for seamounts in the low and  
588 moderate  $Bu$  regimes (Fig. 3j,k), for which the model  
589 diffusivities were underestimated by the scaling of Eq. 1,  
590 and predicts smaller diffusivities than Eq. 1 for Rossby  
591 numbers of order one. A detailed comparison of modelled and  
592 scaling-predicted diffusivities is provided in the Supporting  
593 Information. Although neither scaling fully captures mixing  
594 variability across seamounts, their endorsement by purposeful  
595 (idealized or realistic) numerical simulations authorizes their  
596 use in constructing baseline climatologies of seamount-  
597 generated mixing.

## Global Deep-Ocean Mixing and Upwelling

598 We explore the global implications of seamount-induced  
599 mixing by applying Eq. 1 and Eq. 2 to the KW11  
600 dataset and climatological hydrographic data. Specifically,  
601 we *only* account for the turbulence induced by the shear  
602 and instabilities in the seamount wake ( $Bu > 1$ ), which is  
603 absent from representations of ocean turbulence in climate  
604 models (and hence is the novelty of this work), and not  
605 the mixing associated with seamount-radiated internal lee  
606 waves or (internal tide or lee) wave-vortex interactions, which  
607 can have overlaps with existing mixing estimates. The  
608 outcome of our global diagnostics is shown in Fig. 4a –  
609 the details of the map's construction are discussed in the  
610 Methods and Supporting Information, where we describe the  
611 filtering process employed to ensure that the map produces  
612 a conservative mixing estimate while complying with the  
613 limitations of Eqs. 1 and 2. For comparison, we also show  
614 in Fig. 4c,d estimates of the diffusivity induced by internal  
615 tides (50, 51) and lee waves radiated by abyssal hills (52)

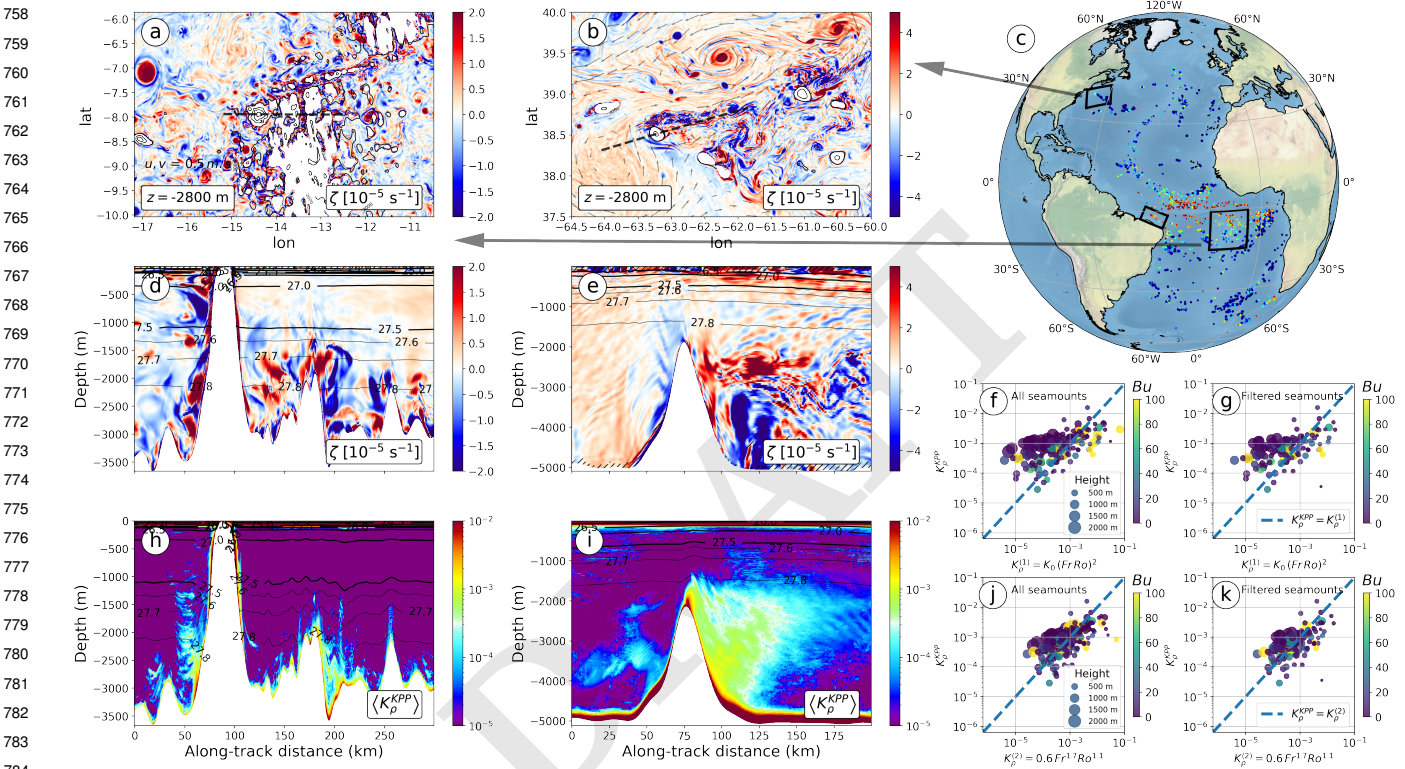
621  
622  
623  
624  
625  
626  
627  
628  
629  
630  
631683  
684  
685  
686  
687  
688  
689  
690  
691  
692  
693

**Fig. 2.** (a,b) Snapshots of relative vorticity (a) at 2800 m depth in the equatorial Atlantic Ocean, and (b) along an approximately along-stream vertical section crossing several seamounts (shown as a dashed line on panel a). Hatched regions highlight instantaneous vertical mixing coefficient  $K_p^{KPP}$  larger than  $10^{-4} \text{ m}^2 \text{s}^{-1}$ . (c) Predicted vertical mixing coefficient  $K_p^{(1)}$  (in  $\text{m}^2 \text{s}^{-1}$ ) based on Eq. 1 and the seamount database following the color scale of panels (f,g). The simulation domain is shown in black. (d) Vertical profiles of  $K_p^{KPP}$  (in  $\text{m}^2 \text{s}^{-1}$ ) spatially integrated over the full simulation domain in blue, over the seamount region in green (see green domain in panel f), and over a region away from seamounts in black. (e) Snapshot of vertical shear of horizontal velocity along the same along-stream vertical section as in (b). (f,g) Time-averaged vertical mixing coefficient  $K_p^{KPP}$  (in  $\text{m}^2 \text{s}^{-1}$ ) (f) at 2800 m depth, and (g) along the same along-stream vertical section as in (b,e).

671  
672  
673  
674  
675  
676  
677  
678  
679  
680  
681  
682727  
728  
729  
730  
731  
732  
733  
734  
735  
736  
737  
738  
739  
740  
741  
742  
743

745  
746  
747  
748  
749  
750  
751  
752  
753  
754  
755  
756  
757

807  
808  
809  
810  
811  
812  
813  
814  
815  
816  
817  
818  
819



788 **Fig. 3.** (a,d) Snapshots of relative vorticity (a) at 2800 m depth over the Mid-Atlantic ridge, and (d) along a vertical section crossing several seamounts (shown as a dashed line in panel a). (b,e) Snapshots of relative vorticity (b) at 2800 m in the North Atlantic and (e) along a vertical section crossing a seamount (shown as a dashed line in panel b). Hatched regions highlight instantaneous diapycnal diffusivities  $K_\rho^{KPP}$  larger than  $10^{-4} \text{ m}^2 \text{ s}^{-1}$ . (c) Predicted diffusivity  $K_\rho^{KPP}$  (in  $\text{m}^2 \text{ s}^{-1}$ ) based on Eq. 1 and the seamount database, following the color scale of panels (h,i). The simulation domains are shown in black. (h,i) Time-averaged diffusivity  $K_\rho^{KPP}$  (in  $\text{m}^2 \text{ s}^{-1}$ ) along the same vertical sections as in (d,e). (f) Scatterplots of modelled diffusivities against predicted diffusivities based on the scaling  $K_\rho^{(1)} = K_0 (Fr Ro)^2$  (predictions based on model parameters) for all seamounts included in the three high-resolution simulation domains shown in panel c. (g) Same as (f) using only seamounts included in the global computation (see Supporting Information). (j,k) Same as (f,g) using the scaling based on a non-linear least squares fit of the model diffusivities:  $K_\rho^{(2)} = K_1 Fr^{1.7} Ro^{1.1}$  with  $K_1 = 0.6 \text{ m}^2 \text{ s}^{-1}$ . The fit was derived using only seamounts included in the global computation; diffusivity is averaged over a cylinder surrounding each seamount and excluding the deepest 100 m of the water column (see Supporting Information).

790  
791  
792  
793  
794  
795  
796  
797  
798  
799  
800  
801  
802  
803  
804  
805  
806

850  
851  
852  
853  
854  
855  
856  
857  
858  
859  
860  
861  
862  
863  
864  
865  
866  
867  
868

along an illustrative abyssal density surface (see Supporting Information for details). Seamount-generated mixing is found to be intense compared to the most energetic tidal and lee wave mixing, especially at lower latitudes, although strong tidal mixing is substantially more widely spread. We stress that the parameterized seamount mixing here only includes the contribution of layered wake vortices and thus excludes tidal or lee wave mixing induced by seamounts. This means there is no overlap between Fig. 4a and Figs. 4c-d, and in theory lee wave mixing from seamounts is not present in either. The map in Fig. 4a is presently absent from mixing parameterizations in ocean and climate general circulation models.

The impact on deep-ocean upwelling of seamount-generated mixing is assessed by quantifying the rate of water mass transformation (53) affected by this and other (*i.e.* internal tides and lee waves) mixing agents. The outcome is shown in Fig. 4e-h. As found by other recent works (1, 2, 54, 55), the net upwelling is the residual of downwelling (prevalent in the interior of basins) and upwelling (focused along topographic boundaries).

Examination of the individual contributions of seamount-, internal tide- and lee wave-generated turbulence to the water mass transformation rate reveals that seamount-induced mixing is a significant player in the net global- or basin-scale diapycnal transfers. For some deep (> 2 km) density classes, seamount-generated mixing contributes O(40%) or larger of the transformation; the tidal component is, of course, expected to be dominant (1, 55). The Pacific Ocean, in particular, seems to host a disproportionately large number of seamounts that can generate layered turbulence (Figs. 1f, 4a). As a result, seamount mixing is plausibly of leading-order importance for the deep Pacific circulation (Fig. 4g-h). Like lee wave-driven mixing (1), the presently estimated seamount mixing causes net buoyancy gain (hence upwelling) within abyssal density classes and net buoyancy loss (downwelling) within overlying layers (Fig. 4f).

We note that the goal of Fig. 4e-h is not to provide a predictive measure of seamount mixing but to show its significant contribution, benchmarked against the much better studied and understood tidal mixing. Much more extensive research and observations are needed before seamount mixing can be accurately quantified on a global scale. Regional observational evidence of energetic turbulent mixing in seamount wakes is currently emerging (56). We suggest that a first step forward would be a comprehensive and accurate identification of seamounts based on recent advancements in seafloor mapping and machine learning methods. The vertical structure of seamount-generated dissipation and mixing also needs scrutiny to go beyond the simple step-like vertical diffusivity profile employed in our global maps (Fig. 4a; Supporting Information).

We emphasize that our estimates are conservative due to three factors: (i) the seamount count of KW11 is very conservative; for example, all three of our regional case studies included many seamounts missing from KW11; (ii) we only accounted for a small fraction of the known seamounts (*e.g.*, compare Fig. 4a with Fig. 1b; see Supporting Information); other seamounts also contribute to mixing; and (iii) we only accounted for shear-induced turbulence in between layered vortical wakes; seamounts are expected to produce additional

mixing via wave generation, wave-vortex interactions, near-boundary instabilities, and tide-seamount interactions, none of which were accounted for here. Furthermore, we restricted the seamount mixing estimates to a narrower volume around the seamounts than one could expect based on our simulations or those upon which Eq. 1 was based.

## Conclusions

We have demonstrated that theoretical descriptions of turbulence generated by flow impingement on seamounts, which were developed under highly idealized scenarios, hold broadly for realistic flow and topography configurations. By conservatively applying these theoretical ideas to global seamount and oceanographic datasets, we have shown that turbulence associated with seamount-generated layered vortices makes an important contribution to deep-ocean mixing and upwelling – comparable to contributions from other, much more extensively studied sources of turbulence. We conclude that seamount-induced turbulence may be a significant new player in the ongoing debate around the closure of the overturning circulation’s deep upwelling limb (8, 30, 58–65). This appears particularly plausible near the equator and in the subtropics, where the layered vortex regime highlighted in our work occurs widely.

Despite this regime’s likely important role in shaping the deep ocean circulation, to our knowledge, there have been no observations of seamount-generated layered vortices and their associated mixing to date. As such, the mixing effects of seamounts are absent from state-of-the-art climate-scale ocean models. Further, one of the largest uncertainties in the estimates presented here is the potentially significant underestimate in the number of seamounts; thus, future improvements to global bathymetric maps will play an important role in quantifying seamount-driven mixing. We suggest that addressing these major knowledge gaps will require not only first-of-their-kind observations (with the deep Pacific as a favoured first candidate, given the expected importance of seamounts in this region) but also advances in dynamical understanding of the evolution of the separated vortices. This evolution may implicate a variety of instabilities (15, 16, 27, 43), as well as interactions with both submesoscale motions at the bottom boundary (17–20) and internal waves (24, 39). Ultimately, integrated measures and parameterizations of mixing accounting for these interacting phenomena are called for to faithfully represent seamount-generated turbulence in climate models.

## Materials and Methods

**Velocity data from the LLC4320 model.** Average flow speeds at the mid-heights of seamounts in the KW11 census are calculated from the LLC4320 model, a global, full-depth ocean and sea ice simulation carried out using the Massachusetts Institute of Technology general circulation model (MITgcm). The model has 1/48° horizontal resolution (0.75 km near Antarctica, 2.3 km at the Equator, and 1 km in the Arctic Ocean) and 90 vertical levels, and has the highest resolution of a hierarchy of simulations that are initialised from a 1/6° global ocean state estimate from the Estimating the Circulation and Climate of the ocean, Phase II, (ECCO2) output (49). The model partially resolves the seamounts of interest here – further discussion of the impact of this and details of the averaging procedure are provided in the Supporting Information. Model descriptions can be found in (34, 66), and

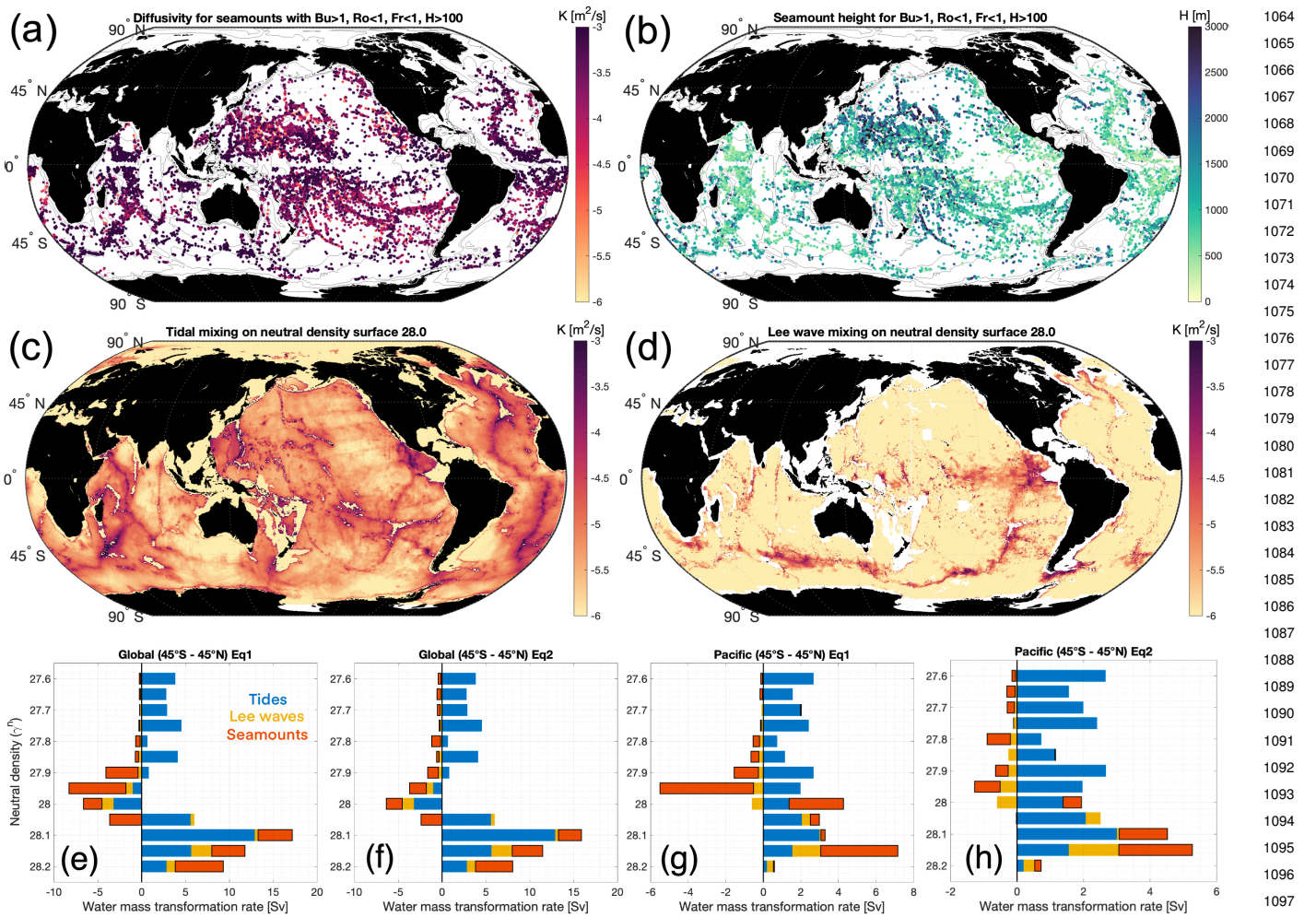


**Fig. 4.** (a) Distribution of seamounts expected to give rise to shear-induced turbulence associated with layered vortices in their wakes ( $Bu > 1$ ). Seamounts with  $Ro > 1$  (too close to the equator and not accounted for in Eq. (1)),  $Fr > 1$  (for which flow is primarily directed over rather than around the seamount), and  $H < 100$  m (fully or partially within the turbulent bottom boundary layer) are all discarded (compare with maps shown in Figure 1). The colour shading indicates the effective turbulent diffusivity ( $\log_{10}$  scale) representing the mixing around and over the height of seamounts, as per Eq. (1). (b) Seamount heights for the seamounts in panel (a). (c) Diapycnal diffusivity ( $\log_{10}$  scale) from tidal mixing on a deep density surface of  $28 \text{ kg m}^{-3}$  with a mean depth of 2000 m and mean height above the bottom of 2160 m (from 50). Diffusivity on a deeper density surface,  $28.1 \text{ kg m}^{-3}$ , is shown in the Supporting Information. (d) Diapycnal diffusivity ( $\log_{10}$  scale) from lee wave mixing on the same density surface as in panel (c) (from 57). (e-h) Water mass transformation rate in the  $45^\circ\text{S} - 45^\circ\text{N}$  global ocean (e,f) and in the  $45^\circ\text{S} - 45^\circ\text{N}$  Pacific Ocean (g,h). We focus on the ocean equatorward of  $45^\circ$  to exclude regions where non-linearities of the equation of state would modify transformation rates significantly (1). In each panel, the net water mass transformation is decomposed into the contributions of (blue) internal tides, (red) seamounts and (yellow) lee waves. Panels (e,g) show contribution due to seamounts calculated based on Eq. 1 and panels (f,h) show the same calculated based on Eq. 2. The former method often yields a larger contribution due to the larger diffusivities associated with high- $Bu$  and  $Ro \sim 1$  flows.

model data are available from the NASA ECCO data portal (<https://data.nas.nasa.gov/ecco/data.php>).

**Regional models.** The three high-resolution regional simulations are performed using the Coastal and Regional Ocean Community model (CROCO), which is built upon the Regional Oceanic Modelling System (ROMS, 67). It solves the free surface, hydrostatic and primitive equations using terrain-following vertical coordinates. The Equatorial domain covers an area of 900 km by 525 km with a horizontal grid spacing of 750 m and 300 vertical levels. The Mid-Atlantic Ridge domain spans an area of 1500 km by 1500 km with a horizontal grid spacing of 1 km and 300 vertical levels. The Gulf Stream domain covers an area of 1000 km by 800 km with a horizontal grid spacing of 500 m and 256 vertical levels. All three domains are initialized and forced at their boundaries using the Atlantic-wide simulation GIGATL3 (68), a realistic simulation spanning the entire Atlantic Basin, performed also using CROCO with a horizontal grid spacing of 3 km and 100 vertical levels during the period 2004–2014. The regional simulations herein correspond to February 2008 to September 2008. The time-mean variables are computed using the last six months of the simulations. Further details on the model simulations are provided in the Supporting Information.

**Global map of seamount diffusivity.** To construct mixing maps based on the layered seamount wake vortices, we first filtered the KW11 data to keep only seamounts with predicted layered dynamics. Estimated diffusivities at each seamount (see Fig. 4a) were computed using the scaling for volume-averaged diffusivity reported in Perfect *et al.* (42) (Eq. (1)), as well as the scaling obtained by fitting diffusivities from the high-resolution realistic simulations described above (Eq. (2)), and applied over a cylinder of radius  $3L$ , where  $L$  is the basal radius, and height equal to that of the seamount. The filtering of seamounts and choice of volume are explained further in the Supporting Information.

**Water mass transformation.** To calculate the water mass transformation rates presented in Figure 4e-h, we used the seamount diffusivities to construct a 2D ‘map’ of mixing on the seafloor on a  $0.5^\circ$  (approximately 50 km) resolution latitude-longitude grid. For each 2D cell, the total mixing was calculated as the sum of that due to all the qualifying seamounts within the cell. We volume-

weighted the diffusivity in each bin by multiplying it by the ratio of the seamount-induced mixing volume and the total cell volume. The mean height of the qualifying seamounts within a cell was also calculated. The 2D map was then translated into a 3D map on the same grid as the WOCE global hydrographic climatology (48): the total mixing in each basal 2D grid cell projected upward using a tanh profile, which is one from the seafloor to a height above the bottom equal to the mean seamount height within the cell and is zero above that. This 3D map of diffusivity was then used with WOCE gridded hydrography to derive water mass transformation rates following (2) (see Supporting Information for more detail).

**ACKNOWLEDGMENTS.** The dataset used to obtain velocities and stratification around seamounts is available at <https://podaac.jpl.nasa.gov/announcements/2021-04-30-Pre-SWOT-L4-Hourly-MITgcm-LLC4320-Native-1/> and <https://data.nas.nasa.gov/ecco/data.php>. Tidal mixing maps are available at <https://doi.org/10.17882/73082>. The seamount parameters calculated based on the LLC4320 and KW11 data are available at <https://zenodo.org/doi/10.5281/zenodo.11145851>; seamount diffusivities shown in Fig 4 can be obtained from this dataset using equations 1 and 2. A.M. acknowledges support from the UK Natural Environment Research Council grant NE/P018319/1 and from the Office of Naval Research grant N00014-22-1-2082. J.G. acknowledges support from the French National Agency for Research (ANR) through the project DEEPER (ANR-19-CE01-0002-01), from PRACE and GENCI for awarding access to HPC resources Joliot-Curie Rome and SKL from GENCI-TGCC (Grants 2022-A0090112051, 2021-A0090112051, 2020-A0090112051, 2019gch0401 and PRACE project 2018194735), and from HPC facilities DATARMOR of “Pôle de Calcul Intensif pour la Mer” at Ifremer Brest

France. L.B. was supported by EPSRC grants EP/L016613/1 and EP/X028135/1, and computational resources provided by the Imperial College London Research Computing Service are gratefully acknowledged (<https://doi.org/10.14469/hpc/2232>). J.J.R. acknowledges support from the Office of Naval Research, Grant N00014-19-1-2154. C.d.L. acknowledges support from the French national LEFE programme through the ROOF project.

1. Casimir De Lavergne, Gurvan Madec, Julien Le Sommer, AJ George Nurser, and Alberto C Naveira Garabato. On the consumption of antarctic bottom water in the abyssal ocean. *Journal of Physical Oceanography*, 46(2):635–661, 2016.
2. Raffaele Ferrari, Ali Mashayek, Trevor J. McDougall, Maxim Nikurashin, and Jean-Michel Campin. Turning ocean mixing upside down. *Journal of Physical Oceanography*, 46(7): 2239–2261, 2016. .

3. S. E. Mikaloff Fletcher, N. Gruber, A. R. Jacobson, S. C. Doney, S. Dutkiewicz, M. Gerber, M. Follows, F. Joos, K. Lindsay, D. Menemenlis, A. Mouchet, S. A. Müller, and J. L. Sarmiento. Inverse estimates of anthropogenic CO<sub>2</sub> uptake, transport, and storage by the ocean. *Global Biogeochem. Cyc.*, 20(2):doi:10.1029/2005GB002530, 2006.
4. A. J. Watson, G. K. Vallis, and M. Nikurashin. Southern ocean buoyancy forcing of ocean ventilation and glacial atmospheric CO<sub>2</sub>. *Nature Geosci.*, 8:861–864, 2015.
5. M. Nikurashin and G. K. Vallis. A theory of the interhemispheric meridional overturning circulation and associated stratification. *J. Phys. Oceanogr.*, 42:1652–1667, 2012.
6. A. F. Thompson, A.L. Stewart, and T. Bischoff. A multi-basin residual-mean model for the global overturning circulation. *J. Phys. Oceanogr.*, 46:2583–2602, 2016.
7. H. F. Drake, R. Ferrari, and J. Callies. Abyssal circulation driven by near-boundary mixing: watermass transformations and interior stratification. *J. Phys. Oceanogr.*, 50:2203–2226, 2020.
8. W. Munk and C. Wunsch. Abyssal recipes II: energetics of tidal and wind mixing. *Deep-Sea Research*, 45:1977–2010, 1998.
9. Caitlin B. Whalen, Casimir de Lavergne, Alberto C. Naveira Garabato, Jody M. Klymak, Jennifer A. MacKinnon, and Katy L. Sheen. Internal wave-driven mixing: governing processes and consequences for climate. *Nature Reviews Earth & Environment*, 1(11): 606–621, 2020. . URL <https://doi.org/10.1038/s43017-020-0097-z>.
10. K. L. Polzin and T. J. McDougall. Mixing at the ocean’s bottom boundary. *Ocean Mixing: Drivers, Mechanisms and Impacts*, pages 145–180, 2021.
11. Larry Armi. Some evidence for boundary mixing in deep ocean. *Journal of Geophysical Research: Oceans*, 83:1971–1979, 1978.
12. Larry Armi. Some evidence for boundary mixing in deep ocean - Reply. *Journal of Geophysical Research: Oceans*, 84:5097–5098, 1979.
13. M. H. Alford, J. B. Girton, G. Voet, G. S. Carter, J. B. Mickett, and Jody M. Klymak. Turbulent mixing and hydraulic control of abyssal water in the samoan passage. *Geophys. Res. Lett.*, 40:4668–4674, 2013.
14. Louis Clément and Andreas M. Thurnherr. Abyssal upwelling in mid-ocean ridge fracture zones. *Geophysical Research Letters*, 45(5):2424–2432, 2018. .
15. M.J. Molemaker, James C. McWilliams, and W.K. Dewar. Submesoscale instability and generation of mesoscale anticyclones near a separation of the California Undercurrent. *J. Phys. Oceanogr.*, 45:613–629, 2015.

- 1241 16. J. Gula, M.J. Molemaker, and James C. McWilliams. Topographic generation of  
1242 submesoscale centrifugal instability and energy dissipation. *Nat. Commu.*, 7:12811, 2016. .  
1243 URL <https://doi.org/10.1175/JPO-D-17-0264.1>.  
1244 17. Jacob O. Wenegrat, Jörn Callies, and Leif N. Thomas. Submesoscale baroclinic instability  
1245 in the bottom boundary layer. *Journal of Physical Oceanography*, 48(11):2571–2592, 2018.  
1246 . URL <https://doi.org/10.1175/JPO-D-17-0264.1>.  
1247 18. Alberto C. Naveira Garabato, Eleanor E. Frajka-Williams, Carl P. Spingys, Sonya Legg,  
1248 Kurt L. Polzin, Alexander Forryan, E. Powl Abrahamsen, Christian E. Buckingham,  
1249 Stephen M. Griffies, Stephen D. McPhail, Keith W. Nicholls, Leif N. Thomas, and Michael P.  
1250 Meredith. Rapid mixing and exchange of deep-ocean waters in an abyssal boundary  
1251 current. *Proceedings of the National Academy of Sciences*, 116(27):13233–13238, 2019.  
1252 ISSN 0027-8424. . URL <https://www.pnas.org/content/116/27/13233>.  
1253 19. Jacob O. Wenegrat and Leif N. Thomas. Centrifugal and symmetric instability during ekman  
1254 adjustment of the bottom boundary layer. *Journal of Physical Oceanography*, 0(0):null,  
1255 2020. . URL <https://doi.org/10.1175/JPO-D-20-0027.1>.  
1256 20. J. Gula, J. Taylor, A. Shcherbina, and A. Mahadevan. *Ocean Mixing: Drivers, Mechanisms  
1257 and Impacts*, chapter Submesoscale processes and Mixing, pages 181–214. Elsevier BV,  
1258 2022.  
1259 21. James C. McWilliams. Submesoscale currents in the ocean. *Proc. R. Soc. A*, 472(2189),  
1260 2016. ISSN 1364-5021. . URL <http://rspa.royalsocietypublishing.org/content/472/2189/20160117>.  
1261 22. C. Vic, G. Roulet, X. Carton, X. Capet, M.J. Molemaker, and J. Gula. Eddy-topography  
1262 interactions and the fate of the Persian Gulf Outflow. *J. Geophys. Res. Oceans*, 120:  
1263 6700–6717, 2015.  
1264 23. W.K. Dewar, M.J. Molemaker, and James C. McWilliams. Centrifugal instability and mixing  
1265 in the California Undercurrent. *J. Phys. Oceanogr.*, 45(12):1244–1241, 2015.  
1266 24. Takeyoshi Nagai, Daisuke Hasegawa, Eisuke Tsutsumi, Hirohiko Nakamura, Ayako Nishina,  
1267 Tomoharu Senju, Takahiro Endoh, Takeshi Matsuno, Ryuichiro Inoue, and Amit Tandon.  
1268 The kuroshio flowing over seamounts and associated submesoscale flows drive  
1269 100-km-wide 100–1000-fold enhancement of turbulence. *Communications Earth &  
1270 Environment*, 2(1):170, 2021. . URL <https://doi.org/10.1038/s43247-021-00230-7>.  
1271 25. C. Z. Lazaneo, P. H. R. Calil, A. Tandon, and I. C. A. da Silveira. Submesoscale coherent  
1272 vortices in the south atlantic ocean: A pathway for energy dissipation. *Journal of  
1273 Geophysical Research: Oceans*, 127(2):e2020JC017099, 2022. . URL  
1274 <https://agupubs.onlinelibrary.wiley.com/doi/abs/10.1029/2020JC017099>. e2020JC017099  
2020JC017099.  
1275 26. B. Perfect, N. Kumar, and J. J. Riley. Vortex structures in the wake of an idealized seamount  
1276 in rotating, stratified flow. *Geophysical Research Letters*, 45(17):9098–9105, 2018. . URL  
1277 <https://agupubs.onlinelibrary.wiley.com/doi/abs/10.1029/2018GL078703>.  
1278 27. Kaushik Srinivasan, James C. McWilliams, M. Jeroen Molemaker, and Roy Barkan.  
1279 Submesoscale vortical wakes in the lee of topography. *Journal of Physical Oceanography*,  
1280 49(7):1949–1971, 2019. . URL <https://doi.org/10.1175/JPO-D-18-0042.1>.  
1281 28. Paul Wessel, David T Sandwell, and Seung-Sep Kim. The global seamount census. *Oceanography*,  
1282 23(1):24–33, 2010.  
1283 29. Chris Yesson, Malcolm R Clark, Michelle L Taylor, and Alex D Rogers. The global  
1284 distribution of seamounts based on 30 arc seconds bathymetry data. *Deep Sea Research Part I: Oceanographic Research Papers*, 58(4):442–453, 2011.  
1285 30. Qian Cao, Changming Dong, Yuxiang Ji, Xingliang Jiang, Brandon J. Bethel, Changshui Xia,  
1286 and Chaochao He. Seamount-induced mixing revealed through idealized experiments and  
1287 its parameterization in an Oceanic General Circulation Model. *Deep Sea Research Part II: Topical Studies in Oceanography*, 202:105144, 2022. ISSN 0967-0645. .  
1288 31. Seung-Sep Kim and Paul Wessel. New global seamount census from altimetry-derived  
1289 gravity data. *Geophysical Journal International*, 186(2):615–631, 2011.  
1290 32. Julie Georgiou, David T. Sandwell, Yao Yu, Seung-Sep Kim, and Paul Wessel. Global  
1291 Distribution and Morphology of Small Seamounts. *Earth and Space Science*, 10(4):  
1292 e2022EA002331, 2023. ISSN 2333-5084. .  
1293 33. John A. Goff and Brian K. Arbic. Global prediction of abyssal hill roughness statistics for  
1294 use in ocean models from digital maps of paleo-spreading rate, paleo-ridge orientation, and  
1295 sediment thickness. *Ocean Modelling*, 33(1-2):36–43, 1 2010. ISSN 1463-5003. . URL  
1296 <https://www.sciencedirect.com/science/article/pii/S1463500309001838>.  
1297 34. Cesar B Rocha, Teresa K Chereskin, Sarah T Gille, and Dimitri Menemenlis. Mesoscale to  
1298 submesoscale wavenumber spectra in drake passage. *Journal of Physical Oceanography*,  
1299 46(2):601–620, 2016.  
1300 35. Brian K Arbic, Matthew H Alford, Joseph K Ansorg, Maarten C Buijsman, Robert B Ciotti,  
1301 J Thomas Farrar, Robert W Hallberg, Christopher E Henze, Christopher N Hill, Conrad A  
1302 Luecke, et al. Primer on global internal tide and internal gravity wave continuum modeling in  
1303 HYCOM and MITgcm. *New frontiers in operational oceanography*, pages 307–392, 2018.  
1304 36. J. Gula, T. M. Blacic, and R. E. Todd. Submesoscale coherent vortices in the Gulf Stream.  
1305 *Geophys. Res. Lett.*, 46, 2019. .  
1306 37. D. C. Napolitano, I. C. A. da Silveira, A. Tandon, and P. H. R. Calil. Submesoscale  
1307 phenomena due to the brazil current crossing of the vitória-trindade ridge. *Journal of  
1308 Geophysical Research: Oceans*, 126(1):e2020JC016731, 2021. . URL  
1309 <https://agupubs.onlinelibrary.wiley.com/doi/abs/10.1029/2020JC016731>. e2020JC016731  
2020JC016731.  
1310 38. Ronald B. Smith. Mountain-induced stagnation points in hydrostatic flow. *Tellus A*, 41 A(3):  
1311 270–274, 1989. ISSN 16000870. .  
1312 39. B. Perfect, N. Kumar, and J. J. Riley. Energetics of seamount wakes. part ii: Wave fluxes.  
1313 *Journal of Physical Oceanography*, 50(5):1383–1398, 2020. . URL  
1314 <https://doi.org/10.1175/JPO-D-19-0104.1>.  
1315 40. MG Wurtele, RD Sharman, and A Datta. Atmospheric lee waves. *Annual review of fluid  
1316 mechanics*, 28(1):429–476, 1996.  
1317 41. Ronald B Smith. 100 years of progress on mountain meteorology research. *Meteorological  
1318 Monographs*, 59:20–1, 2019.  
1319 42. B. Perfect, N. Kumar, and J. J. Riley. Energetics of seamount wakes. part i: Energy  
1320 exchange. *Journal of Physical Oceanography*, 50(5):1365–1382, 2020. . URL  
1321 https://doi.org/10.1175/JPO-D-19-0105.1.  
1322 43. Kaushik Srinivasan, James C. McWilliams, and Arjun Jagannathan. High vertical shear and  
1323 dissipation in equatorial topographic wakes. *Journal of Physical Oceanography*, 2021. .  
1324 URL <https://journals.ametsoc.org/view/journals/phoc/aop/JPO-D-20-0119.1/JPO-D-20-0119.1.xml>.  
1325 44. M Nikurashin and R Ferrari. Global energy conversion rate from geostrophic flows into  
1326 internal lee waves in the deep ocean. *Geophysical Research Letters*, 38(8):L08610, 2011.  
1327 45. A. C. Naveira Garabato, A. J. G. Nurser, R. B. Scott, and J. A. Goff. The impact of  
1328 small-scale topography on the dynamical balance of the ocean. *J. Phys. Oceanogr.*, 43:  
1329 647–668, 2013.  
1330 46. Eric Kunze and John M Toole. Tidally driven vorticity, diurnal shear, and turbulence atop  
1331 fierberling seamount. *Journal of Physical Oceanography*, 27(12):2663–2693, 1997.  
1332 47. Pranav Puthan, Geno Pawlak, and Sutanu Sarkar. Wake Vortices and Dissipation in a  
1333 Tidally Modulated Flow Past a Three-Dimensional Topography. *Journal of Geophysical  
1334 Research: Oceans*, 127(8):e2022JC018470, 2022. ISSN 2169-9291. .  
1335 48. V Gouretski and K P Koltermann. WOCE global hydrographic climatology. *Berichte des  
1336 BSH*, 35:1–52, 2004.  
1337 49. D. Menemenlis, J. Campin, P. Heimbach, C. Hill, T. Lee, A. Nguyen, M. Schodlock, and  
1338 H. Zhang. Ecco2: High resolution global ocean and sea ice data synthesis. *Mercator Ocean  
1339 Quart. Newslett.*, 31:13–21, 2008.  
1340 50. Casimir de Lavergne, Clément Vic, Gurvan Madec, Fabien Roquet, Amy F Waterhouse,  
1341 CB Whalen, Yannis Cuypers, Pascale Bouruet-Aubertot, Bruno Ferron, and Toshiyuki  
1342 Hibiya. A parameterization of local and remote tidal mixing. *Journal of Advances in  
1343 Modeling Earth Systems*, 12(5):e2020MS002065, 2020.  
1344 51. C de Lavergne, C Vic, G Madec, F Roquet, AF Waterhouse, CB Whalen, and Y Cuypers.  
1345 Global tidal mixing maps. *SEANOE*, 10:73082, 2020.  
1346 52. M. Nikurashin and R. Ferrari. Global energy conversion rate from geostrophic flows into  
1347 internal lee waves in the deep ocean. *Geophys. Res. Lett.*, 38:L08610, 2011. .  
1348 53. Sjoerd Groeskamp, Stephen M. Griffies, Danièle Judicone, Robert Marsh, A. J. George  
1349 Nurser, and Jan D. Zika. The water mass transformation framework for ocean physics and  
1350 biogeochemistry. *Annual Review of Marine Science*, 11:271–305, 2019. ISSN 19410611. .  
1351 54. A Mashayek, H Salehipour, D Bouffard, C P Caulfield, R Ferrari, M Nikurashin, W R Peltier,  
1352 and W D Smyth. Efficiency of turbulent mixing in the abyssal ocean circulation. *Geophysical  
1353 Research Letters*, 44(12):6296–6306, 2017.  
1354 55. Laura Cimoli, Colm-cille P. Caulfield, Helen L. Johnson, David P. Marshall, Ali Mashayek,  
1355 Alberto C. Naveira Garabato, and Clément Vic. Sensitivity of Deep Ocean Mixing to Local  
1356 Internal Tide Breaking and Mixing Efficiency. *Geophysical Research Letters*, 46(24):  
1357 14622–14633, 12 2019. ISSN 0904-8276. . URL  
1358 <https://onlinelibrary.wiley.com/doi/abs/10.1029/2019GL085056>.  
1359 56. Anne Takahashi, Ren-Chieh Lien, Eric Kunze, Barry Ma, Hirohiko Nakamura, Ayako  
1360 Nishina, Eisuke Tsutsumi, Ryuichiro Inoue, Takeyoshi Nagai, and Takahiro Endoh.  
1361 Energetic stratified turbulence generated by kuroshio-seamount interactions in tokara strait.  
1362 *Journal of Physical Oceanography*, 2023.  
1363 57. M. Nikurashin and R. Ferrari. Overturning circulation driven by breaking internal waves in  
1364 the deep ocean. *Geophysical Research Letters*, 40(12):3133–3137, 2013. ISSN 1944-8007.  
1365 . URL <http://dx.doi.org/10.1002/grl.50542>.  
1366 58. Lynne Talley, Joseph L. Reid, and Paul E Robbins. Data-based meridional overturning  
1367 streamfunctions for the global ocean. *Journal of Climate*, 16(19):3213–3226, 2003.  
1368 59. C Wunsch and R Ferrari. Vertical mixing, energy, and the general circulation of the oceans.  
1369 *Annu. Rev. Fluid Mech.*, 36:281–314, 2004.  
1370 60. R Lumpkin and K Speer. Global ocean meridional overturning. *Journal of Physical  
1371 Oceanography*, 37(10):2550–2562, 2007.  
1372 61. Lynne Talley. Closure of the Global Overturning Circulation Through the Indian, Pacific, and  
1373 Southern Oceans: Schematics and Transports. *Oceanography*, 26(1):80–97, 3 2013. ISSN  
1374 1042875. . URL <https://tos.org/oceanography/article/closure-of-the-global-overturning-circulation-through-the-indian-pacific-an>.  
1375 62. Amy F Waterhouse, Jennifer A Mackinnon, Jonathan D Nash, Matthew H Alford, Eric  
1376 Kunze, Harper L Simmons, Kurt L Polzin, Louis C St. Laurent, Oliver M Sun, Robert Pinkel,  
1377 and others. Global patterns of diapycnal mixing from measurements of the turbulent  
1378 dissipation rate. *Journal of Physical Oceanography*, 44(7):1854–1872, 2014.  
1379 63. Raffaele Ferrari. Oceanography: What goes down must come up. *Nature*, 513(7517):  
1380 179–180, 2014.  
1381 64. T.N. Huussen, A.C. Naveira-Garabato, H.L. Bryden, and E.L. McDonagh. Is the deep indian  
1382 ocean MOC sustained by breaking internal waves? *Journal of Geophysical Research: Oceans*,  
1383 117, 2012.  
1384 65. Laura Cimoli et al. Significance of diapycnal mixing within the Atlantic Meridional  
1385 Overturning Circulation. *Nature Communications*, 2021.  
1386 66. Zhan Su, Jinbo Wang, Patrice Klein, Andrew F Thompson, and Dimitris Menemenlis. Ocean  
1387 submesoscales as a key component of the global heat budget. *Nature communications*, 9  
1388 (1):1–8, 2018.  
1389 67. A.F. Shchepetkin and James C. McWilliams. The Regional Oceanic Modeling System  
1390 (ROMS): A split-explicit, free-surface, topography-following- coordinate ocean model.  
1391 *Ocean Modelling*, 9:347–404, 2005.  
1392 68. Jonathan Gula, Sébastien Theetten, Gildas Cambon, and Guillaume Roulet. Description of  
1393 the GIGATL simulations, June 2021. URL <https://doi.org/10.5281/zenodo.4948523>.  
1394 . URL <https://doi.org/10.1175/JPO-D-19-0104.1>.  
1395 69. M. Nikurashin and R. Ferrari. Global energy conversion rate from geostrophic flows into  
1396 internal lee waves in the deep ocean. *Geophysical Research Letters*, 38:L08610, 2011. .  
1397 70. Lynne Talley. Closure of the Global Overturning Circulation Through the Indian, Pacific, and  
1398 Southern Oceans: Schematics and Transports. *Oceanography*, 26(1):80–97, 3 2013. ISSN  
1399 1042875. . URL <https://tos.org/oceanography/article/closure-of-the-global-overturning-circulation-through-the-indian-pacific-an>.  
1400 71. Amy F Waterhouse, Jennifer A Mackinnon, Jonathan D Nash, Matthew H Alford, Eric  
1401 Kunze, Harper L Simmons, Kurt L Polzin, Louis C St. Laurent, Oliver M Sun, Robert Pinkel,  
1402 and others. Global patterns of diapycnal mixing from measurements of the turbulent  
1403 dissipation rate. *Journal of Physical Oceanography*, 44(7):1854–1872, 2014.  
1404 72. Raffaele Ferrari. Oceanography: What goes down must come up. *Nature*, 513(7517):  
1405 179–180, 2014.  
1406 73. T.N. Huussen, A.C. Naveira-Garabato, H.L. Bryden, and E.L. McDonagh. Is the deep indian  
1407 ocean MOC sustained by breaking internal waves? *Journal of Geophysical Research: Oceans*,  
1408 117, 2012.  
1409 74. Laura Cimoli et al. Significance of diapycnal mixing within the Atlantic Meridional  
1410 Overturning Circulation. *Nature Communications*, 2021.  
1411 75. Zhan Su, Jinbo Wang, Patrice Klein, Andrew F Thompson, and Dimitris Menemenlis. Ocean  
1412 submesoscales as a key component of the global heat budget. *Nature communications*, 9  
1413 (1):1–8, 2018.  
1414 76. A.F. Shchepetkin and James C. McWilliams. The Regional Oceanic Modeling System  
1415 (ROMS): A split-explicit, free-surface, topography-following- coordinate ocean model.  
1416 *Ocean Modelling*, 9:347–404, 2005.  
1417 77. Jonathan Gula, Sébastien Theetten, Gildas Cambon, and Guillaume Roulet. Description of  
1418 the GIGATL simulations, June 2021. URL <https://doi.org/10.5281/zenodo.4948523>.  
1419 . URL <https://doi.org/10.1175/JPO-D-19-0104.1>.  
1420 78. M. Nikurashin and R. Ferrari. Global energy conversion rate from geostrophic flows into  
1421 internal lee waves in the deep ocean. *Geophysical Research Letters*, 38:L08610, 2011. .  
1422 79. Lynne Talley. Closure of the Global Overturning Circulation Through the Indian, Pacific, and  
1423 Southern Oceans: Schematics and Transports. *Oceanography*, 26(1):80–97, 3 2013. ISSN  
1424 1042875. . URL <https://tos.org/oceanography/article/closure-of-the-global-overturning-circulation-through-the-indian-pacific-an>.  
1425 80. Amy F Waterhouse, Jennifer A Mackinnon, Jonathan D Nash, Matthew H Alford, Eric  
1426 Kunze, Harper L Simmons, Kurt L Polzin, Louis C St. Laurent, Oliver M Sun, Robert Pinkel,  
1427 and others. Global patterns of diapycnal mixing from measurements of the turbulent  
1428 dissipation rate. *Journal of Physical Oceanography*, 44(7):1854–1872, 2014.  
1429 81. Raffaele Ferrari. Oceanography: What goes down must come up. *Nature*, 513(7517):  
1430 179–180, 2014.  
1431 82. T.N. HuusSEN, A.C. Naveira-Garabato, H.L. Bryden, and E.L. McDonagh. Is the deep indian  
1432 ocean MOC sustained by breaking internal waves? *Journal of Geophysical Research: Oceans*,  
1433 117, 2012.  
1434 83. Laura Cimoli et al. Significance of diapycnal mixing within the Atlantic Meridional  
1435 Overturning Circulation. *Nature Communications*, 2021.  
1436 84. Zhan Su, Jinbo Wang, Patrice Klein, Andrew F Thompson, and Dimitris Menemenlis. Ocean  
1437 submesoscales as a key component of the global heat budget. *Nature communications*, 9  
1438 (1):1–8, 2018.  
1439 85. A.F. Shchepetkin and James C. McWilliams. The Regional Oceanic Modeling System  
1440 (ROMS): A split-explicit, free-surface, topography-following- coordinate ocean model.  
1441 *Ocean Modelling*, 9:347–404, 2005.  
1442 86. Jonathan Gula, Sébastien Theetten, Gildas Cambon, and Guillaume Roulet. Description of  
1443 the GIGATL simulations, June 2021. URL <https://doi.org/10.5281/zenodo.4948523>.  
1444 . URL <https://doi.org/10.1175/JPO-D-19-0104.1>.  
1445 87. M. Nikurashin and R. Ferrari. Global energy conversion rate from geostrophic flows into  
1446 internal lee waves in the deep ocean. *Geophysical Research Letters*, 38:L08610, 2011. .  
1447 88. Lynne Talley. Closure of the Global Overturning Circulation Through the Indian, Pacific, and  
1448 Southern Oceans: Schematics and Transports. *Oceanography*, 26(1):80–97, 3 2013. ISSN  
1449 1042875. . URL <https://tos.org/oceanography/article/closure-of-the-global-overturning-circulation-through-the-indian-pacific-an>.  
1450 89. Amy F Waterhouse, Jennifer A Mackinnon, Jonathan D Nash, Matthew H Alford, Eric  
1451 Kunze, Harper L Simmons, Kurt L Polzin, Louis C St. Laurent, Oliver M Sun, Robert Pinkel,  
1452 and others. Global patterns of diapycnal mixing from measurements of the turbulent  
1453 dissipation rate. *Journal of Physical Oceanography*, 44(7):1854–1872, 2014.  
1454 90. Raffaele Ferrari. Oceanography: What goes down must come up. *Nature*, 513(7517):  
1455 179–180, 2014.  
1456 91. T.N. HuusSEN, A.C. Naveira-Garabato, H.L. Bryden, and E.L. McDonagh. Is the deep indian  
1457 ocean MOC sustained by breaking internal waves? *Journal of Geophysical Research: Oceans*,  
1458 117, 2012.  
1459 92. Laura Cimoli et al. Significance of diapycnal mixing within the Atlantic Meridional  
1460 Overturning Circulation. *Nature Communications*, 2021.  
1461 93. Zhan Su, Jinbo Wang, Patrice Klein, Andrew F Thompson, and Dimitris Menemenlis. Ocean  
1462 submesoscales as a key component of the global heat budget. *Nature communications*, 9  
1463 (1):1–8, 2018.  
1464 94. A.F. Shchepetkin and James C. McWilliams. The Regional Oceanic Modeling System  
1465 (ROMS): A split-explicit, free-surface, topography-following- coordinate ocean model.  
1466 *Ocean Modelling*, 9:347–404, 2005.  
1467 95. Jonathan Gula, Sébastien Theetten, Gildas Cambon, and Guillaume Roulet. Description of  
1468 the GIGATL simulations, June 2021. URL <https://doi.org/10.5281/zenodo.4948523>.  
1469 . URL <https://doi.org/10.1175/JPO-D-19-0104.1>.  
1470 96. M. Nikurashin and R. Ferrari. Global energy conversion rate from geostrophic flows into  
1471 internal lee waves in the deep ocean. *Geophysical Research Letters*, 38:L08610, 2011. .  
1472 97. Lynne Talley. Closure of the Global Overturning Circulation Through the Indian, Pacific, and  
1473 Southern Oceans: Schematics and Transports. *Oceanography*, 26(1):80–97, 3 2013. ISSN  
1474 1042875. . URL <https://tos.org/oceanography/article/closure-of-the-global-overturning-circulation-through-the-indian-pacific-an>.  
1475 98. Amy F Waterhouse, Jennifer A Mackinnon, Jonathan D Nash, Matthew H Alford, Eric  
1476 Kunze, Harper L Simmons, Kurt L Polzin, Louis C St. Laurent, Oliver M Sun, Robert Pinkel,  
1477 and others. Global patterns of diapycnal mixing from measurements of the turbulent  
1478 dissipation rate. *Journal of Physical Oceanography*, 44(7):1854–1872, 2014.  
1479 99. Raffaele Ferrari. Oceanography: What goes down must come up. *Nature*, 513(7517):  
1480 179–180, 2014.  
1481 100. T.N. HuusSEN, A.C. Naveira-Garabato, H.L. Bryden, and E.L. McDonagh. Is the deep indian  
1482 ocean MOC sustained by breaking internal waves? *Journal of Geophysical Research: Oceans*,  
1483 117, 2012.  
1484 101. Laura Cimoli et al. Significance of diapycnal mixing within the Atlantic Meridional  
1485 Overturning Circulation. *Nature Communications*, 2021.  
1486 102. Zhan Su, Jinbo Wang, Patrice Klein, Andrew F Thompson, and Dimitris Menemenlis. Ocean  
1487 submesoscales as a key component of the global heat budget. *Nature communications*, 9  
1488 (1):1–8, 2018.  
1489 103. A.F. Shchepetkin and James C. McWilliams. The Regional Oceanic Modeling System  
1490 (ROMS): A split-explicit, free-surface, topography-following- coordinate ocean model.  
1491 *Ocean Modelling*, 9:347–404, 2005.  
1492 104. Jonathan Gula, Sébastien Theetten, Gildas Cambon, and Guillaume Roulet. Description of  
1493 the GIGATL simulations, June 2021. URL <https://doi.org/10.5281/zenodo.4948523>.  
1494 . URL <https://doi.org/10.1175/JPO-D-19-0104.1>.  
1495 105. M. Nikurashin and R. Ferrari. Global energy conversion rate from geostrophic flows into  
1496 internal lee waves in the deep ocean. *Geophysical Research Letters*, 38:L08610, 2011. .  
1497 106. Lynne Talley. Closure of the Global Overturning Circulation Through the Indian, Pacific, and  
1498 Southern Oceans: Schematics and Transports. *Oceanography*, 26(1):80–97, 3 2013. ISSN  
1499 1042875. . URL <https://tos.org/oceanography/article/closure-of-the-global-overturning-circulation-through-the-indian-pacific-an>.  
1500 107. Amy F Waterhouse, Jennifer A Mackinnon, Jonathan D Nash, Matthew H Alford, Eric  
1501 Kunze, Harper L Simmons, Kurt L Polzin, Louis C St. Laurent, Oliver M Sun, Robert Pinkel,  
1502 and others. Global patterns of diapycnal mixing from measurements of the turbulent  
1503 dissipation rate. *Journal of Physical Oceanography*, 44(7):1854–1872, 2014.  
1504 108. Raffaele Ferrari. Oceanography: What goes down must come up. *Nature*, 513(7517):  
1505 179–180, 2014.  
1506 109. T.N. HuusSEN, A.C. Naveira-Garabato, H.L. Bryden, and E.L. McDonagh. Is the deep indian  
1507 ocean MOC sustained by breaking internal waves? *Journal of Geophysical Research: Oceans*,  
1508 117, 2012.  
1509 110. Laura Cimoli et al. Significance of diapycnal mixing within the Atlantic Meridional  
1510 Overturning Circulation. *Nature Communications*, 2021.  
1511 111. Zhan Su, Jinbo Wang, Patrice Klein, Andrew F Thompson, and Dimitris Menemenlis. Ocean  
1512 submesoscales as a key component of the global heat budget. *Nature communications*, 9  
1513 (1):1–8, 2018.  
1514 112. A.F. Shchepetkin and James C. McWilliams. The Regional Oceanic Modeling System  
1515 (ROMS): A split-explicit, free-surface, topography-following- coordinate ocean model.  
1516 *Ocean Modelling*, 9:347–404, 2005.  
1517 113. Jonathan Gula, Sébastien Theetten, Gildas Cambon, and Guillaume Roulet. Description of  
1518 the GIGATL simulations, June 2021. URL <https://doi.org/10.5281/zenodo.4948523>.  
1519 . URL <https://doi.org/10.1175/JPO-D-19-0104.1>.  
1520 114. M. Nikurashin and R. Ferrari. Global energy conversion rate from geostrophic flows into  
1521 internal lee waves in the deep ocean. *Geophysical Research Letters*, 38:L08610, 2011. .  
1522 115. Lynne Talley. Closure of the Global Overturning Circulation Through the Indian, Pacific, and  
1523 Southern Oceans: Schematics and Transports. *Oceanography*, 26(1):80–97, 3 2013. ISSN  
1524 1042875. . URL <https://tos.org/oceanography/article/closure-of-the-global-overturning-circulation-through-the-indian-pacific-an>.  
1525 116. Amy F Waterhouse, Jennifer A Mackinnon, Jonathan D Nash, Matthew H Alford, Eric  
1526 Kunze, Harper L Simmons, Kurt L Polzin, Louis C St. Laurent, Oliver M Sun, Robert Pinkel,  
1527 and others. Global patterns of diapycnal mixing from measurements of the turbulent  
1528 dissipation rate. *Journal of Physical Oceanography*, 44(7):1854–1872, 2014.  
1529 117. Raffaele Ferrari. Oceanography: What goes down must come up. *Nature*, 513(7517):  
1530 179–180, 2014.  
1531 118. T.N. HuusSEN